Protein Conformations Explored by Difference High-Angle Solution X-ray Scattering: Oxidation State and Temperature Dependent Changes in Cytochrome C†

David M. Tiede,* Ruitian Zhang, and Soenke Seifert

Chemistry Division, Argonne National Laboratory, Argonne, Illinois 60439

Received November 12, 2001; Revised Manuscript Received March 23, 2002

ABSTRACT: We demonstrate the use of high-angle X-ray scattering to explore protein conformational states in solution by resolving oxidation state- and temperature-dependent changes in the conformation of horse heart cytochrome *c*. Several detailed models exist for oxidation-dependent changes in mitochondrial class I *c* cytochromes determined by X-ray crystallography and solution NMR techniques. These models differ in the magnitude and locations of structural change. Our scattering measurements show that high-angle X-ray scattering can discriminate between these models, and that the experimental scattering data for horse cytochrome *c* can be best reconciled with selected NMR models for the same protein. These results demonstrate the ability to use high-angle X-ray scattering to resolve conformational states of proteins in solution, and to relate these measurements to detailed structural models. Furthermore, temperature-dependent changes are found in the high angle scattering patterns for horse cytochrome *c*, illustrating the sensitivity of these measurements to dynamic aspects of protein structure. These results demonstrate the ability to use difference high angle scattering as a quantitative monitor of reaction-linked changes in protein conformation and structural dynamics. Synchrotron-based high-angle scattering holds promise as a widely applicable, high throughput technique for exploring conformational states linked to physiological protein function, for resolving configurational differences between protein structures in solution and crystalline states, and for bridging the gap between solution NMR and crystallographic structure techniques.

A central issue in structural biology lies in identifying the range of configurational substates accessible to proteins under physiological conditions and correlating these structural variations to biological function (*1*, *2*). Protein structure determination by X-ray crystallography and solution NMR differ in their ability to resolve structural variation. Crystallography is inherently restricted to structure determination under the set of conditions compatible with crystallization. For protein molecules positioned at equivalent positions in a unit cell, a single structure is resolved, and configurational variability is expressed in the crystallographic B-factor. Subtle structure differences are frequently resolved for protein molecules occupying inequivalent positions in the unit cell (e.g., *3*), implying that crystallographic packing can at least alter the very fine structure of proteins (or vice versa). In contrast, structure determination by solution NMR yields an ensemble of structures, frequently with a structural variation that exceeds the uncertainty represented by the crystallographic B-factors (*4*, *5*). While general agreement is usually found in overall protein structure measured by crystallographic and NMR methods, structural models determined by the two methods frequently differ in the details of protein structure, particularly in loop and protein turn regions that are potentially significant for understanding biological function. In this paper, we have explored the use of high-angle X-ray scattering as a means to detect reaction-linked changes in protein structure, and to discriminate between crystallographic and NMR models. Oxidation state-dependent conformational changes in cytochrome *c* have been investigated as a test system.

Oxidation state-dependent changes in class I *c* cytochrome structures have been extensively studied. Resolution of oxidation state-dependent changes in cytochrome *c* structure is significant for understanding the role of these configurational changes in electron-transfer function, for example, in resolving the source of the thermodynamic reorganization energy during electron transfer (*6*, *7*), and for understanding the factors that control the dramatic oxidation state-dependent change in cytochrome *c* stability and dynamics (*8*−*10*).

Crystallographic studies have found that only subtle structural differences are linked to oxidation state changes in cytochrome *c*. For example, a comparison of the oxidized and reduced yeast iso-1-cytochrome *c* crystal structures showed a small, 0.3 Å rms difference in protein backbone atom positions that is distributed roughly uniformly throughout the protein (*11*). Individual side chain positions were found to show larger positional variance (up to 4 Å variation) for a small number of residues, primarily restricted to the region surrounding the heme (*11*). The oxidation state-dependent structural change has been found to be even smaller in crystallographic studies of class I bacterial cytochromes *c* (*3*, *12*, *13*).

In contrast, much larger oxidation state-dependent changes in cytochrome *c* structure have been reported from solution

† Supported by the Office of Basic Energy Sciences, Divisions of Chemical and Material Sciences, U.S. Department of Energy, under contract W-31-109-ENG-38.

* Corresponding author: D. M. Tiede, Chemistry Division D-200, Argonne National Laboratory, 9700 South Cass Ave., Argonne, IL 60439. E-mail: tiede@anl.gov.

10.1021/bi015931h CCC: $22.00
Published on Web 05/02/2002

NMR studies. For example, an early NMR structure determination of horse cytochrome *c* detected a 2.4 Å rms difference in backbone atoms positions between oxidized and reduced states (*14*). The variation included changes in α-helix and protein secondary structures. In a more recent, higher-resolution NMR study of the horse cytochrome, a smaller oxidation state-dependent change in structure was seen, corresponding to a 1.4 Å rms variation in backbone atom position, which arose primarily from loop regions (*15*, *16*). A comparison of the crystallographic and NMR studies indicates the need to reconcile the NMR and crystallographic views of reaction linked structural change.

Recently, considerable success has been achieved in the ab initio determination of macromolecular shape from synchrotron X-ray scattering data for a variety of proteins and nucleotide-protein complexes in solution, using small angle scattering patterns as fitting criteria in global configurational searches (*17*−*23*). These procedures produce low resolution models of protein structure, either by reconstructing macromolecular shapes from a series of spherical harmonics (*18*, *24*), or by packing of spheres of uniform electron density (*20*, *21*). These methods have achieved macromolecular shape reconstruction with 2-nm resolution (*18*, *21*, *25*), and recent work suggests that scattering patterns contain information on the shape of proteins up to a resolution of about 0.5 nm (*26*).

The availability of high-flux, third generation synchrotron X-ray sources and the development of large area solid-state detectors have opened up new opportunities for collecting high-precision, high-angle X-ray scattering patterns for proteins in solution (*27*). The opportunity to detect high-angle scattering is significant since it probes distance correlations on length scales that are small compared to the macromolecular dimensions, and potentially contains information on the details of protein structure in solution (*28*, *29*). Methods have been developed for accurately calculating scattering patterns for proteins based on atomic coordinates (*30*). We have recently extended the numerical precision of these techniques to allow accurate calculation of protein scattering based on atomic coordinates to high angle, and included Debye−Waller expressions to account for the effects of thermal factors (*31*). This work has shown that high-angle scattering data is sensitive to the details of protein folding and dynamic properties (*26*, *31*, *32*).

In this paper, we have tested the idea of using high-angle scattering to detect conformational states of proteins by examining oxidation state- and temperature-dependent changes in cytochrome *c*. The advantages of the scattering technique are that it is fast, applicable to a variety of physiologically relevant solution conditions, including the variation of temperature, pH, ionic strength, substrates, etc., and is quantitatively relatable to single crystal diffraction. Furthermore, high-angle scattering measurements provide a useful complement to NMR measurements. Both techniques use comparable samples, but scattering provides a global measure of all atom−atom distance correlations, while NMR provides a high-resolution determination of a selected subset of atom−atom distances. Therefore, solution scattering potentially affords a significant adjunct to structure studies by providing a means to explore protein conformation states in solution in a manner quantitatively relatable to detailed structural models, and to serve as a bridge between high-resolution crystallographic and solution NMR studies. In this paper, we have measured oxidation state- and temperature-dependent changes in cytochrome *c* solution scattering, and compared these to scattering patterns calculated from crystallographic and NMR models.

MATERIALS AND METHODS

Sample Preparation. Horse cytochrome *c* (MW = 12 384) was obtained from Sigma (type VI) and freshly prepared just prior to use as 4 mM solutions (50 mg/mL) in a variety of buffers (10 mM HEPES, pH 7.2, 10 mM Tris, pH 7.8, 10 mM phosphate, pH 7.0) and ionic strengths (0−250 mM NaCl). These conditions are comparable to those used for solution structure determination of horse cytochrome *c* by NMR techniques (*14*−*16*). In some experiments, scattering measurements were made using horse cytochrome *c* that had been further purified by ionic exchange chromatography on a cationic exchange resin Sephacel CM 52. Differences in scattering pattering patterns were not detected between the samples used as received from Sigma, and those purified by additional chromatography.

X-ray Scattering Measurements. Initial X-ray scattering experiments were performed at beam line 4-2 at the Stanford Synchrotron Research Laboratory (SSRL). Subsequent experiments were carried out at the BESSRC beam line 12-ID of the Advanced Photon Source (APS) at Argonne National Laboratory. The X-ray wavelength was set at $\lambda = 1.378$ Å (SSRL) and 0.949 Å (APS) by double-crystal Si(111) monochromators. Scattered X-rays were collected using a linear wire detector (BioLogic, Grenoble, France) at SSRL and a two-dimensional mosaic CCD detector (*27*) at APS. The sample-to-detector distances were set such that the detecting range for momentum transfer were $0.02 < q < 0.8$ Å^{-1}, where $q = (4\pi/\lambda)\ sin\ \theta$, and λ is the X-ray wavelength and 2θ is the scattering angle. Transmission coefficients of the samples and solution backgrounds were measured either using an air-filled gas detector placed at the exit window of the sample holder (SSRL) or using a PIN-diode mounted on the beam stop (APS) (*27*). Beam defining slits at APS were adjusted to yield a 0.5 × 0.3 mm beam cross section at the sample. A pneumatic shutter synchronized to the CCD detector data acquisition gated sample X-ray exposure (*27*). Apart from the improved signal-to-noise and shorter data acquisition times obtained at APS, the scattering patterns collected from each X-ray source were indistinguishable.

Scattering patterns were collected using sample flow cells to avoid radiation damage during data acquisition. Two designs were used. A single chamber version was constructed from 1.5-mm-thick Lucite, with a 2 × 5 mm scattering chamber covered with 25 μm mica windows (Goodfellow). Checks for sample integrity and radiation damage were made by monitoring the UV−Vis optical absorption of the sample, measured using a pair of 100 μm optical fibers placed in the flow path just after the X-ray scattering chamber, and coupled to a tungsten−halogen light source and CCD-based spectrometer (Ocean Optics). The light emitting and receiving optical fibers were positioned with a spacing of about 100 μm to permit measurement of the optical absorption spectra of the 4 mM cytochrome *c* solutions (molar absorptivity, reduced cytochrome *c*, 550 nm = 28 mM^{-1} cm $^{-1}$).

Measurements at APS showed evidence for radiation damage after 20 s of exposure, detectable in optical absorption spectra by the appearance of 630 nm absorption peak characteristic of a disrupted His/Met cytochrome *c* heme axial iron ligation scheme, and detected in scattering patterns by an increase low *q* scattering intensity and a broadening of high *q* features. The deleterious effects of radiation exposure were found to be eliminated by flowing the samples with flow rates in the range 20 to 50 μL/min. On the basis of the approximately 0.3-mm beam height at APS and the dimensions of the sample cell, these flow rates correspond to X-ray exposure times of 3 to 1.2 s, respectively, during continuous data acquisition. The independence of the cytochrome optical spectra and X-ray scattering patterns with flow rates in this range indicates that the sample exposure times were sufficiently short to avoid radiation damage.

A two chamber flow cell, fabricated from stainless steel with mica windows, was used to minimize the effects of slight variations in the background scattering pattern detected during the time course of data acquisition. A dual syringe pump was used to drive protein and buffer background solutions through each sample chamber. Scattering data was collected using an automated data acquisition cycle, consisting of a shuttered 2-D scattering image acquisition from the first chamber, a 4 s delay while the image file was saved to disk, and a stepping motor repositioned the sample cell to center the second chamber in the beam path, followed by an equivalent shuttered 2-D scattering image acquisition from the second chamber and subsequent file save and sample repositioning. The 2-D image acquisition times were adjusted, typically in the range 8−10 s, to keep all pixels of the charge accumulating CCD detector below saturation. Scattering patterns were accumulated following 10−12 data acquisition cycles, corresponding to total data acquisition times of 80−120 s.

Temperature control was obtained by mounting the two chamber stainless steel flow cell on a 9 × 9 mm thermoelectric cooler (Melcor). Temperature control of ±0.1 °C was achieved in the temperature region −10−100 °C.

The 2-D scattering images were corrected for spacial distortion and sensitivity, and then were radially averaged to produce 1-D map of scattered intensity versus *q*. The scattering profile, $I(q)$, for cytochrome *c* was obtained by averaging the difference between successive pairs of 1-D measurements of scattered intensities measured for the cytochrome *c* solution and the solution background in the data acquisition sequence. The error bars represent the standard deviation measured between successive pairs of data acquisition cycles.

Calculated Scattering Patterns. Solution scattering is a function of the macromolecule concentration, *n*, the macromolecular form factor, $P(q)$, and the solution structure factor, $S(q)$:

$$I(q) = nP(q)S(q) \tag{1}$$

The form factor accounts for all contributions linked to the structure of the macromolecule in solution, and it is the component of primary concern in this report. Structure factors in solution arise from nonrandom, or correlated particle−particle distributions produced by interparticle interactions, and modulate the observed scattering profile (*33*−*35*). Experimentally, the modulation effect of the structure factor was minimized by finding ionic strength and counterion conditions that screen the interparticle electrostatic coupling, as described in the results. Under these conditions, $S(q) \approx 1$, and the experimental scattering patterns can be compared to form factors calculated from atomic coordinates.

Procedures for calculating scattering patterns from atomic coordinates followed those developed by Svergun (*30*), but were extended using numerical precision sufficient to permit accurate calculation of solution scattering to high angle ($q < 2$ Å^{-1}) (*31*). In this approach, protein scattering is calculated from the orientational average of partial scattering amplitudes arising from the fixed atomic coordinates, A_a, the solvent excluded volume, A_s:

$$P(\boldsymbol{q}) = \langle |A_a(\boldsymbol{q}) - A_s(\boldsymbol{q})|^2 \rangle_\Omega \tag{2}$$

where Ω represents the unit solid angle. Previous studies also examined the effect of a hydration layer (*30*) that was not included in the present analysis. The coherent scattering amplitude from the protein included effects of the Debye−Waller atomic fluctuation factor (*36*), and was calculated as follows:

$$A_a(\boldsymbol{q}) = \rho_0 \sum_{j=1}^{N} f_j(\boldsymbol{q}) e^{i\boldsymbol{q}\cdot\boldsymbol{r}_j} e^{-B_j q^2/16\pi^2} \tag{3}$$

where f_j is the atomic form factor, B_j is the Debye−Waller B-factor, and *N* is the total number of non-hydrogen atoms (*31*). Hydrogen atoms, which make a significant contribution to the total macromolecular scattering were grouped to the corresponding non-hydrogen atoms. The form factor f_j for the group is calculated from the group atomic geometry. The Debye−Waller B-factor is proportional to the mean square positional fluctuation, and is proportional to the absolute temperature.

The solvent excluded volume was approximated by the dummy atom model (*30*, *37*). The total scattering amplitude for the dummy atoms is

$$A_s(\boldsymbol{q}) = \rho_0 \sum_{j=1}^{N} g_j(\boldsymbol{q}) e^{i\boldsymbol{q}\cdot r_j} \tag{4}$$

where ρ_0 is solvent electron density, and g_j is the form factor for the dummy atom, or group of atoms, with volume V_j:

$$g_j(\boldsymbol{q}) = G(\boldsymbol{q}) V_j e^{-q^2 V_j^{2/3}/4\pi} \tag{5}$$

and $G(\boldsymbol{q})$ is a volume expansion factor (*30*) written as:

$$G(\mathbf{q}) = \frac{V_o}{V_m} \mathrm{e}^{-q^2(V_o^{2/3} - V_m^{2/3})/4\pi} \tag{6}$$

where V_o is the expanded atomic volume, and V_m is the average atomic volume for the group. The expansion factor $G(\mathbf{q})$ is useful, for example, to account for imperfect packing of solvent molecules around the atomic groups. The expansion factor is adjusted by changing the ratio of the dummy atom radius to average atomic radius, r_o/r_m, typically in the range 1.01 to 1.03. Using these procedures, we have demonstrated the sensitivity of calculated wide-angle scat-

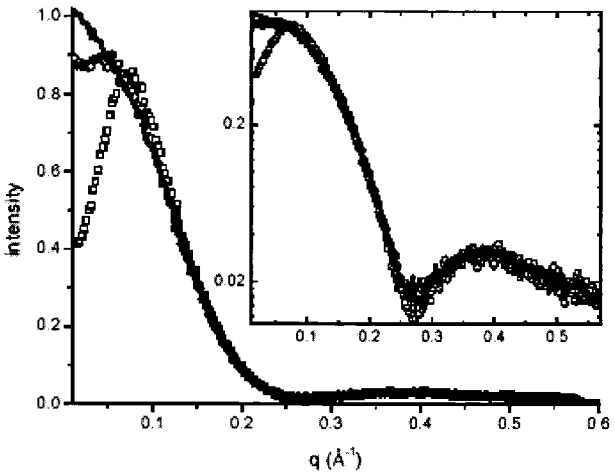

FIGURE 1: Effect of ionic strength and counterion on X-ray scattering for horse cytochrome *c*. Scattering patterns are shown for 4 mM cytochrome *c* solutions in 10 mM Hepes, 10 mM sodium acetate, pH 7.2 (□), 10 mM sodium phosphate, pH 7.2 (○), and 10 mM Hepes, 250 mM NaCl, pH 7.2 (—). These scattering patterns were measured at SSRL, Stanford University, using a sample flow rate of 50 μL/min, and exposure time of 500 s.

tering patterns to the details of protein structure and atomic temperature factors (*31*).

Calculation of oxidation state-dependent changes in cytochrome *c* scattering were based upon structures in the Protein Data Bank (*38*). Crystallographic structures for oxidized and reduced yeast iso-1-cytochrome *c* (*11*, *39*) were taken from the Protein Data Bank entries 1cty and 1ctz, respectively. Two sets of structures are available for oxidized and reduced horse cytochrome *c* in solution, determined using NMR techniques. Scattering patterns were calculated from *1akk*, *1giw* (*15*, *16*), and *1ocd*, *2frc* (*14*). Crystallographic structures for horse cytochrome *c* are only available for the oxidized state. Calculations presented here used the *1hrc* entry, determined using X-ray crystallography (*40*).

RESULTS

Interparticle Interactions. Previous work has shown that prominent, electrostatically based, repulsive interparticle interactions significantly distort solution X-ray scattering patterns for horse heart cytochrome *c* in a concentration-dependent manner (*41*). These effects are clearly evident in scattering patterns measured for cytochrome *c* in low ionic strength buffers, and with the 4 mM cytochrome *c*oncentration used in the present investigation to get good signal-to-noise in the high angle region. For example, the trace marked by filled squares in Figure 1 shows the scattering pattern measured for 4 mM cytochrome *c* in 10 mM Hepes, pH 7.2, with 10 mM sodium acetate. The scattering pattern shows a prominent peak in scattered intensity at $q = 0.074$ Å^{-1} and significantly reduced scattered intensity at lower angles. The amplitude and position of the peak in scattering intensity arise as a consequence of nonrandom, particle distribution in solution, characterized by the solution structure factor, that arises because of significant, repulsive interparticle interaction (*41*). We have found that the strength of this interaction potential is strongly modulated by the nature of the anion, and the ionic strength. For example, replacing 10 mM sodium acetate with 10 mM sodium phosphate significantly reduces the amplitude of the peak in scattered intensity, and shifts it toward smaller q. These effects can be understood to reflect a reduction in the mean force interaction potential (*34*, *41*), and can be correlated with charge compensation by the known selective anion binding properties of cytochrome *c* (*42*). At higher ionic strength, electrostatic screening effectively reduces the interaction to the point where scattering patterns accurately reflect the cytochrome form factor (i.e., $I(q) = nP(q)S(q)$, where $S(q) \rightarrow 1$). This can be illustrated by the scattering pattern measured for horse cytochrome *c* with 100 mM sodium chloride (solid line trace in Figure 1). Guinier analysis (*43*) of the scattering data yields an R_g of 12.8 ± 0.2 Å, which is comparable to the 12.6 Å calculated (*30*, *31*) from the crystal coordinates (*40*). In the following experiments, cytochrome *c* scattering was measured in 0.25 M NaCl to minimize the effects of interparticle interaction on cytochrome *c* scattering patterns.

These measurements of cytochrome scattering patterns as a function of ionic strength have shown that variation in the interparticle interaction does not significantly alter high angle scattering data. This is illustrated by the inset in Figure 1, where scattered intensity is plotted on a logarithmic scale, permitting a comparison of both high and low angle scattered intensities. The data shows that although the interparticle interactions are significantly modulated by changes in the ionic composition of the solutions, the scattering data at higher angle ($q > 0.2$ Å^{-1}) are not detectably altered. These results demonstrate that with the high ionic strength solutions used in the following experiments, the high angle scattering measurements reliably reflect the particle form factor and are not detectably distorted by interference with solution structure factors.

High Angle Scattering. The sensitivity of high angle scattering to the details of protein structure can be tested in a preliminary way by comparing scattering patterns for proteins with different folding motifs. Figure 2 shows experimental and calculated scattering patterns for three test proteins, lysozyme, myoglobin, and horse cytochrome *c*. The high angle scattering patterns for all three proteins show broad oscillatory features that are distinguishable and that are in reasonable agreement with theoretical scattering patterns calculated from crystal coordinates. The experimental scattering data for lysozyme and myoglobin deviate from their calculated patterns at low angle, reflecting attractive interparticle interactions that have not been minimized in our experimental conditions (*34*).

The simulation of experimental high angle scattering based on scattering patterns calculated from crystal coordinates required the effects of atomic motion to be taken into account (*31*, *44*). This was accomplished in a manner analogous to the treatment of thermal disorder in crystallography, by including an angle-dependent weighting of the scattering contribution from each atom with a Debye factor (*36*). In these simulations, the weighting was calculated using the crystallographic B-factors, multiplied by a common scaling factor for B that was adjusted to approximate the experimental data. The modulation of the amplitude of the temperature factor was found to primarily affect the slope of the diffuse scattering at higher angle ($q > 0.3$ Å^{-1}), but had negligible effect on the small angle scattering signal (*31*, *44*). We have found that the scaling factor required to match calculated and experimental high angle scattering data differs for individual proteins. For example, the calculated scattering

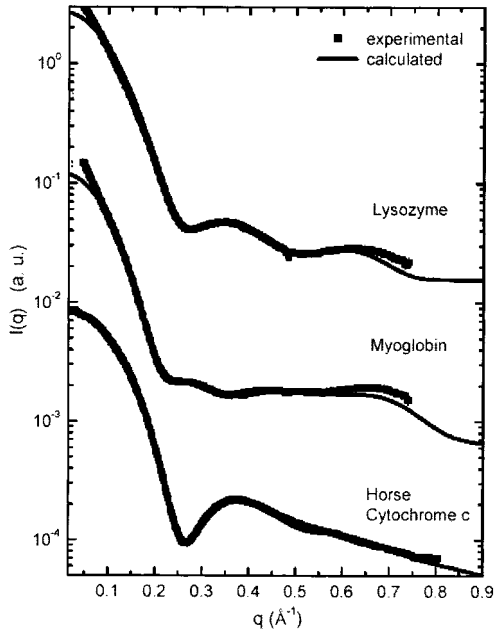

FIGURE 2: Comparison of experimental and calculated X-ray scattering patterns for lysozyme, myoglobin, and horse cytochrome *c*. Experimental scattering patterns were measured with protein concentrations of 10 mg/mL for lysozyme and myoglobin and 50 mg/mL for cytochrome *c*. The buffer solution was 10 mM Hepes, 250 mM NaCl, pH 7.2 for each protein sample. Data acquisition times were 200 s for lysozyme and myoglobin and 96 s for cytochrome *c*, using a sample flow rate of 50 μL/min for each case. Data were collected at the BESSRC beam line, APS, Argonne National Laboratory. Scattering patterns were calculated from crystal coordinates, using the protein data bank entry *6lyz* for hen egg-white lysozyme (*51*), *1ymb*, for horse metmyoglobin (*52*), and *1hrc* for oxidized horse cytochrome *c* (*40*). The dummy atom expansion factor, r_o/r_m, used for the lysozyme and myoglobin calculated scattering patterns was 1.02, and 1.03 was used for the cytochrome calculation. The calculated patterns used the crystallographic temperature factors, scaled by 1 for lysozyme and myoglobin, and scaled by 3 for cytochrome *c*. Experimental data are marked by the solid symbol (■) and calculated patterns are indicated by the solid line (—).

patterns for lysozyme and myoglobin in Figure 2 both used the B-factors contained in the crystallographic files. In contrast, the correspondence between the experimental and calculated scattering patterns for horse cytochrome *c* required that the crystallographic B-factors be multiplied by a factor of 3. Furthermore, we have noted that even within the highly homologous set of mitochondrial *c* cytochromes, the details of the high angle scattering patterns are distinguishable, and that these proteins vary in the parameters needed to find agreement between the experimental and calculated scattering patterns (D. Tiede and R. Zhang, unpublished). These findings indicate that high angle scattering patterns are sensitive to the dynamic nature of protein structures, and that these motions vary significantly within a set of homologous proteins. Atomic fluctuations considered here are only the first in a hierarchy of motions that can be expected to affect high angle protein scattering (*36*, *45*, *46*−*48*), and the present treatment should be considered as a preliminary approach. A more detailed consideration of the thermal factors required for simulation of high *q* scattering for these proteins will be presented elsewhere. The main point that we wish to make here is that these scattering measurements have shown that distinguishable protein structures exhibit characteristic high angle scattering patterns, and that these high angle experimental scattering patterns can be reasonably accounted by calculation from crystal coordinate data provided that thermal factors are also taken into account. These findings suggest that the high angle scattering data contains information on the protein folding pattern and structural dynamics, and that there is opportunity to make quantitative comparison between experimental solution scattering data and detailed structural models.

Oxidation-Dependent Changes in High Angle Scattering. The oxidation state induced changes in cytochrome *c* provide a useful test of the sensitivity of high angle X-ray scattering to reaction-linked changes in protein fine structure. Three different high-resolution structural models exist for oxidation state-dependent changes in mitochondrial class I type *c* cytochromes. One is based upon crystallographic data for yeast cytochrome *c* (*11*), and two models have been determined for horse cytochrome *c* in solution using NMR techniques (*14*−*16*). Figure 3 shows backbone atom traces for these oxidized and reduced cytochrome *c* structures, rotated to superimpose the heme coordinates. The crystallographic studies of yeast cytochrome *c* found that the oxidized and reduced structures are nearly overlapping (Figure 3a) having only a small, 0.3 Å rms difference in protein backbone atoms positions. Much larger structural changes were measured for horse cytochrome *c* in solution, with a more recent study (*15*, *16*) finding a 1.4 Å rms difference in backbone atom positions between the average oxidized and reduced structures (Figure 3b), while an earlier study (*14*) found a 2.4 Å rms difference between the average structures, Figure 3c. The differences between these structural models suggest that either the horse and yeast cytochromes differ in their oxidation state-dependent change, or that significant differences exist between the oxidation state-dependent change in crystals and solution.

Scattering calculations based upon these structural models suggests that high angle scattering measurements can resolve subtle oxidation state differences if measured with sufficient precision. For example, the lower pair of traces in Figure 4 shows the scattering patterns calculated using the oxidized and reduced yeast crystallographic coordinates and B-factors. At small angle, $q < 0.2$ Å^{-1}, the two calculated traces are found to be indistinguishable, but slight deviations are seen in the calculated scattering patterns at high angle. The difference scattering pattern is shown by the solid line trace in Figure 5, plotted as the percentage change in scattered intensity. The difference scattering pattern calculated from the oxidized and reduced yeast cytochrome *c* coordinates shows broad oscillatory features with a maximum amplitude corresponding to about a 5% change in scattered intensity.

Scattering patterns were also calculated for oxidized and reduced horse heart cytochrome *c* structures determined by solution NMR (*14*−*16*). For example, the upper pair of traces in Figure 4 shows the scattering patterns calculated from the ensemble-averaged oxidized and reduced structures most recently determined by NMR (*15*, *16*). Again, scattering patterns calculated from the oxidized and reduced horse cytochrome *c* structures were found to be indistinguishable at low angle, $q < 0.2$ Å^{-1}, but significant differences are seen at high angle. The difference scattering pattern is plotted in Figure 5, dashed line. The difference scattering pattern calculated from the horse cytochrome solution structures is clearly distinguishable from that calculated from the yeast

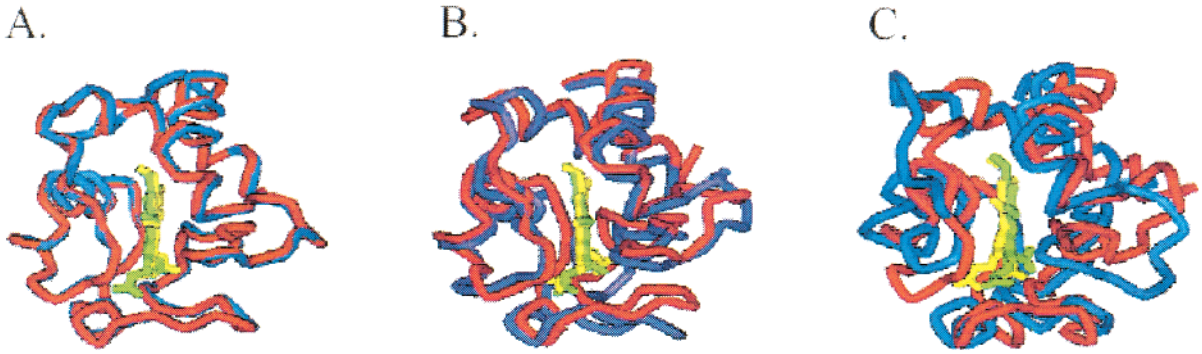

FIGURE 3: Comparison of oxidation state-dependent structural change for eucaryotic cytochrome *c* measured by X-ray crystallography and solution NMR. The backbone atom positions are shown for the oxidized cytochrome in red and the reduced cytochrome in blue, with the two coordinate systems rotated to superimpose the heme group. Part A shows the crystallographic structures for yeast iso-1-cytochrome *c* (*11*), using Protein Data Bank entries *1cty* and *1ctz*. Part B shows the averaged, energy-minimized solution NMR structures determined for horse cytochrome *c* (*15*, *16*), using entries *1akk* and *1giw*. Part C shows the averaged, energy minimized solution NMR structures determined for horse cytochrome *c* (*14*) using protein data bank entries *1ocd* and *2frc*. Structures were displayed using WebLab ViewerLite (Accelrys).

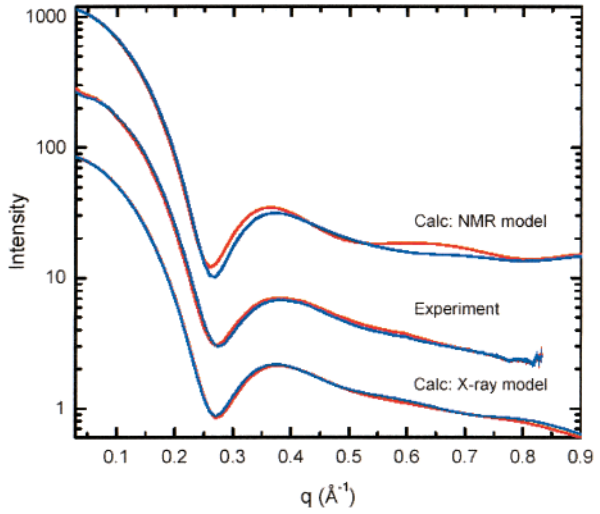

FIGURE 4: Comparison of experimental and calculated scattering patterns for oxidized and reduced cytochrome *c*. The top pair of traces shows scattering patterns calculated from the averaged, energy minimized NMR structures *1akk* and *1giw* (*15*, *16*). The middle pair of traces shows the experimental scattering patterns measured for oxidized and reduced horse heart cytochrome *c* measured as described in Figure 2. The lower pair of traces shows scattering patterns calculated for the oxidized and reduced X-ray crystal structures *1cty* and *1ctz* for yeast iso-1-cytochrome *c* (*11*). Oxidized and reduced scattering patterns are shown in red and blue, respectively.

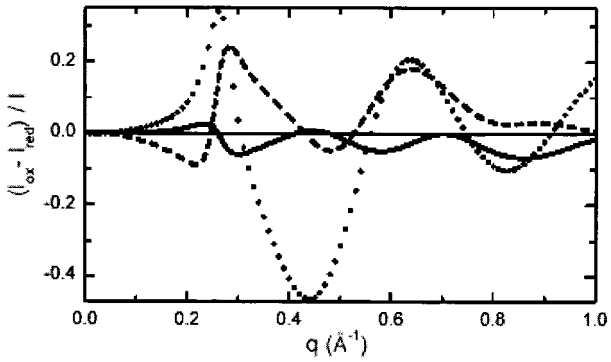

FIGURE 5: Oxidized-minus-reduced difference scattering patterns calculated from crystallographic and NMR models. The solid line shows the difference pattern calculated from the yeast iso-1-cytochrome *c* structures (*11*). The dashed and dotted lines show difference patterns calculated for horse cytochrome structures determined in solution by NMR by Banci et al. (*15*, *16*) and Qi et al. (*14*), respectively. The amplitudes are plotted as the percent change in scattered intensity.

crystal structures. The horse difference pattern shows a high peak amplitude, corresponding to an approximate 25% change in scattered intensity at $q = 0.28$ Å^{-1}. The difference scattering pattern was also calculated from the earlier NMR models for horse cytochrome *c* (*14*), and is plotted as the dotted line trace in Figure 5. Comparison of the scattering patterns calculated from all three models for the oxidation state-dependent structural change in cytochrome *c* shows that the magnitude of the high angle scattering change increases with structural divergence, and that the high angle scattering pattern is remarkably sensitive to even the relatively small structural changes (0.3 Å rms difference in backbone atom positions) detected in the yeast crystal structures.

We have measured very high precision high angle scattering patterns for cytochrome *c* by taking advantage of a third generation synchrotron source (*27*). The middle pair of traces in Figure 4 shows experimental scattering patterns measured for oxidized and reduced horse cytochrome *c*, each recorded at the BESSRC (12-ID) beamline at APS with 96 s of acquisition time. Evidence for radiation damage was carefully monitored and reduced to negligible levels by flowing the samples as described in the methods. The high X-ray flux at APS permitted very high precision measurements. The experimental error bars are plotted in the figure, but for most data points the statistical variation is smaller than the thickness of the plotted line. For example, the average standard deviation measured with respect to the amplitude of scattering in the region $0.2 < q < 0.6$ Å^{-1} was 0.45%. Hence, the experimental difference scattering patterns can be measured with sufficient precision to resolve even the small oxidation state-dependent changes predicted from crystallographic models. The subtle oxidation state-dependent changes in the experimental high angle scattering for cytochrome *c* were found to be highly reproducible, and comparable difference scattering patterns were recorded at APS and SSRL synchrotron sources, although the high flux at APS offers the advantage of permitting much shorter data acquisition times.

The experimental difference scattering pattern for horse cytochrome *c* is plotted in Figure 6, along with the calculated difference scattering patterns from the crystallographic and recent NMR models. The comparison shows that the

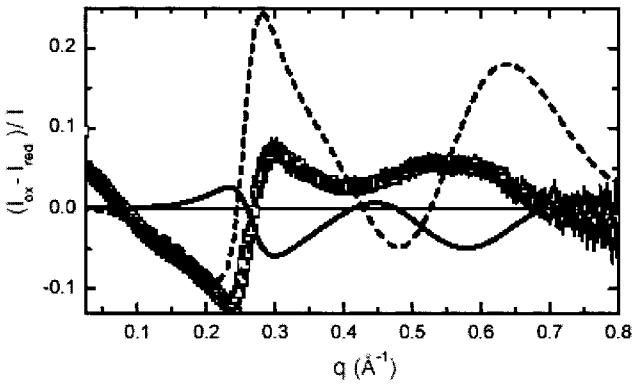

FIGURE 6: Comparison of experimental and calculated oxidized-minus-reduced difference scattering patterns. The experimental difference pattern (□) is the difference between the scattering patterns measured for oxidized and reduced horse cytochrome *c* shown in Figure 4. The solid and dashed lines are the difference scattering patterns calculated from the crystallographic and NMR models shown in Figure 4.

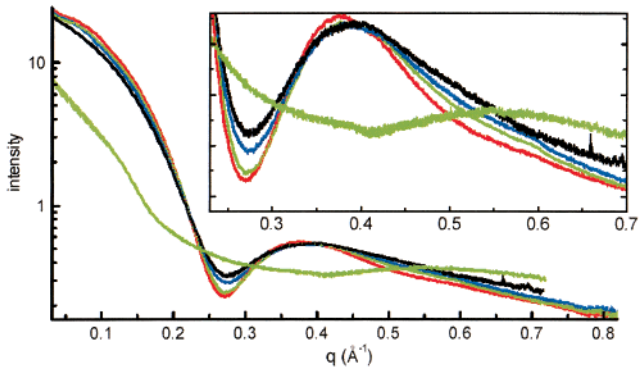

FIGURE 7: Temperature-dependent changes in X-ray solution scattering for oxidized horse cytochrome *c*. The scattering patterns show a progression change with temperature. Traces are plotted for 2 °C (red), 40 °C (green), 50 °C (blue), 60 °C (black), and 72 °C (green). In the high *q* region (inset), the 2 °C trace shows the deepest minimum at $q = 0.27$ Å^{-1} and lowest amplitude of diffuse scattering with $q > 0.4$ Å^{-1}. The order of amplitudes is reversed in the low *q* (<0.2 Å^{-1}) region. Experimental conditionals were as described in Figure 2.

experimental difference scattering pattern is in good agreement with neither model, although the general shape of the experimental difference pattern is more similar to that calculated from the NMR model. However, the amplitudes of the positive features of the experimental difference pattern are about 3-fold smaller than those calculated from the NMR models, and there is an appreciable mismatch in the position of the second positive peak. In contrast, the amplitudes of the peaks in the experimental difference pattern are found to be larger than those calculated from the yeast crystallographic coordinates, and of opposite sign.

A major factor affecting the comparison between scattering patterns calculated from the NMR models and the experimental data is the unweighted averaging of structures across the NMR ensembles. The coordinates for the ensemble have only been deposited for the reduced form of horse cytochrome *c* (*15*, *16*). We have found that scattering patterns calculated for individual structures within this ensemble show a wide variation, with only a subset of the structures being compatible with experimental scattering data. In addition, discrepancies between experiment and the NMR models were found to be greater for the average ensemble-averaged oxidized horse structure compared to the reduced one. This can be seen from an inspection of Figure 4. Specifically, the scattering pattern calculated from the oxidized cytochrome NMR structure shows scattered intensities near $q = 0.3$ Å^{-1} and $q = 0.65$ Å^{-1} that are in excess of that seen in experiment. These peaks are the positions of major discrepancy in the comparison of experimental and calculated oxidation state-dependent difference patterns, Figure 6. These observations suggest that it is primarily the oxidized horse cytochrome *c* structure that is responsible for the discrepancies in oxidation state-dependent changes seen between experiment and model-based calculations.

Temperature-Dependent Changes in High Angle Scattering. The experiments described above demonstrate the sensitivity of high angle X-ray scattering patterns to relatively subtle reaction-linked structural change in cytochrome *c*, and suggest the feasibility of using high angle scattering as a means to discriminate between models for protein conformational states in solution. The sensitivity of high angle scattering to changes in protein conformation can also be tested by examining the effect of temperature. Temperature can be expected to alter the population of conformational substates, and to affect the dynamics of interconversion between these states. An understanding of how these protein dynamics are manifest in high angle scattering is important for developing accurate, quantitative methods for calculating X-ray scattering data based upon molecular models.

Figure 7 shows the scattering patterns measured for horse cytochrome *c* as function of temperature between 1 and 80 °C. As the temperature is raised from 1 to 60 °C, the scattering patterns show a progressive, reversible conversion that includes a change in the shape of the low *q* scattering, $q < 0.2$ Å^{-1}, a loss in the depth of the minimum seen at $q = 0.27$ Å^{-1}, and a progressive increase in the diffuse scattering at $q > 0.4$ Å^{-1}. Abrupt, irreversible changes occur in the scattering patterns above 60 °C, which presumably reflects denaturation of the protein.

The reversible changes in scattering seen in the temperature region 1−60 °C are significant since they potentially reflect transitions between configurational states related to the folded, native structure. Scattering difference patterns are plotted in Figure 8, showing the characteristic temperature-induced changes. The top panel, Figure 8, shows the 2−25 °C, 40−25 °C, and 50−25 °C difference patterns for oxidized cytochrome *c*. Prominent features include the peak at $q = 0.27$ Å^{-1} due to the loss of the depth of the first minimum, the peak near $q = 0.55$ Å^{-1} due to the progressive change in the shape of the secondary maximum, and the increase in the diffuse scattering at $q > 0.55$ Å^{-1}. The changes in the scattering seen between 2 and 25 °C are significant since they indicate that even room temperature scattering patterns are influenced by the accessibility of thermally populated configurations. The middle panel, Figure 8, compares the 2−25 °C difference scattering pattern for oxidized and reduced cytochrome *c*. The close correspondence demonstrates the reproducibility of the measurement, and the similarity in temperature-dependent changes in protein conformation for both oxidation states of cytochrome *c*. The bottom panel, Figure 8, compares the 2−25 °C difference scattering pattern with the oxidized-reduced difference scattering pattern. These data show that both the oxidation state

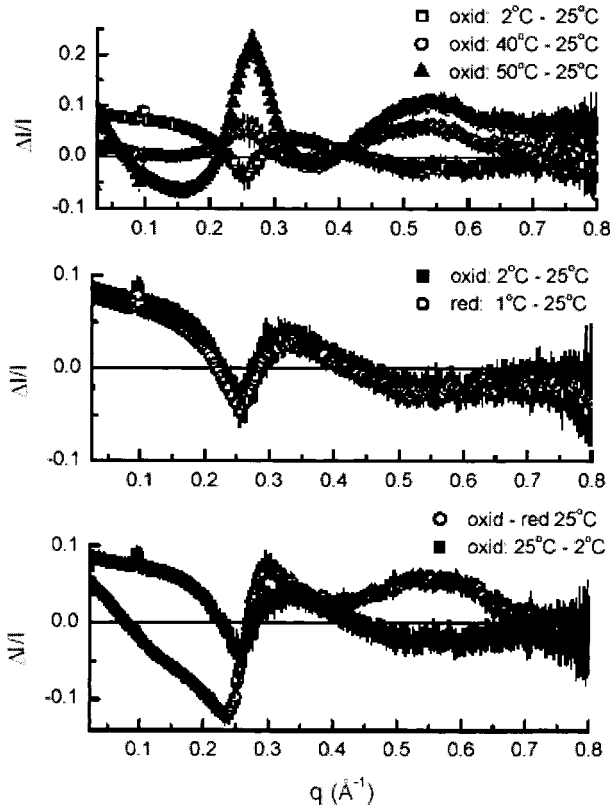

FIGURE 8: Temperature-dependent difference X-ray scattering patterns for horse cytochrome *c*. The top panel shows the 2 °C minus 25 °C (□), 40° minus 25 °C (○), and 50 minus 25 °C (▲) difference scattering patterns measured for oxidized cytochrome *c*. The middle panel compares the 2 minus 25 °C (■) and 1 minus 25 °C (○) differences scattering patterns measured for oxidized and reduced cytochrome *c*, respectively. The lower panel compares oxidation state- and temperature-induced difference scattering patterns. The oxidized-minus-reduced difference scattering pattern measured at 25 °C is marked by the open symbol (○), and the 2 minus 25 °C measured for oxidized cytochrome *c* is marked by the filled symbol (■).

and temperature produce characteristic, clearly distinguishable changes in scattering.

DISCUSSION

In this paper, we have demonstrated that high-precision, high angle X-ray scattering measurements provide a sensitive monitor of protein conformation that can be quantitatively compared to crystallographic or NMR structural models. This was demonstrated by resolving difference X-ray scattering patterns associated with subtle, oxidation state-dependent changes in cytochrome *c* fine structure. X-ray scattering is fundamentally rooted in orientationally averaged atomic scattering. By basing the analysis of macromolecular high angle scattering on atomic scattering (*28*−*30*), and by including the effects of thermal factors (*31*, *32*), high angle scattering becomes a direct measure of structural change that can be quantitatively related to structural models. In particular, we have found that the shapes of difference high angle scattering patterns calculated from models of oxidation-dependent conformational change in cytochrome *c* are distinguishable, and depend on both the sites and magnitudes of structural change. Hence, while we emphasize that analysis of solution scattering data alone cannot unambiguously lead to the determination of a single unique detailed structure, it can identify which of several competing structural models are consistent with experimental data. This can be important, for example, in distinguishing between NMR and crystallographic models for protein structure in solution. Difference high angle scattering is a widely applicable technique for exploring protein conformation in a variety of solution conditions, potentially applicable in a high-throughput manner at third-generation synchrotron sources. We anticipate that the high angle scattering technique will have application in a number of areas that include (i) testing for the applicability of the sometimes differing details of crystallographic and NMR models to solution states of proteins, (ii) provide a method for extending crystallographic models to fit scattering data recorded under a range of physiologically relevant solution conditions not addressable by crystallography, and hence provide a method for identifying conformationally distinct structural states relevant to physiological function, and (iii) extend the accuracy of NMR structural determination by providing a method to discriminate between protein conformers not distinguished by NMR data alone.

Reaction-Linked Changes in Changes in Cytochrome c. Oxidation state-dependent changes in cytochrome *c* structure provide a useful model for calibrating the sensitivity of high angle X-ray scattering to subtle reaction-linked structural change. Three detailed models exist for oxidation state-dependent changes in class I, mitochondrial *c*-type cytochromes. The crystallographic models for yeast cytochrome *c* (Y67F, C102T double mutant) show the smallest oxidation state-dependent change, characterized by a 0.3 Å rms change in backbone atom positions (*11*). NMR analysis for horse cytochrome *c* in solution shows a larger 1.4 Å rms oxidation state change in backbone atom positions (*15*, *16*). An earlier NMR analysis of horse cytochrome *c* found a larger 2.4 Å rms difference (*14*). Difference scattering patterns calculated from these models show that the magnitude of the high angle difference scattering increases with structural disparity between the oxidized and reduced states, and that remarkably, even the subtle reorganization measured in the yeast crystals can be detected with high precision high angle scattering measurements. As outlined in the results, the experimental difference scattering patterns for horse cytochrome *c* are in best agreement with the more recent NMR horse cytochrome structures (*15*, *16*), particularly by considering that major differences between the experimental and calculated difference scattering patterns are likely to arise from discrepancies with the averaged oxidized structure. This finding suggests that a quantitative comparison between NMR models and high angle scattering data will require a detailed comparison between experimental data and scattering patterns calculated for each of the structures within the NMR ensembles. The ensemble of structures is currently available only for the reduced horse cytochrome (*15*, *16*). Preliminary analysis of scattering patterns calculated from individual conformers within this ensemble show a wide variation in agreement with experimental scattering data (D. Tiede and R. Zhang, unpublished), suggesting that it is possible to use high angle scattering data to determine weighting factors for the contribution of individual conformers to solution scattering.

Calculation of difference scattering patterns based on each of the three models for oxidation state-dependent change in

cytochrome *c* show that the reaction linked structural change is best resolved in high angle scattering region, with negligible changes predicted to be detected in the small angle scattering region ($q \leq R_g^{-1}$). This result can be understood from the fact that high angle scattering probes short-range atomic distance correlations that are expected to be a more sensitive monitor of internal atomic reorganization than are the overall size and shape parameters detected by small angle scattering. However, experiments show that small, oxidation state-dependent variations are also seen in the small angle data. These observations are in agreement with earlier studies that showed an oxidation state-dependent change in the apparent R_g measured for horse cytochrome *c* in solution (*8*). The finding that high angle difference patterns can be explained by models for internal atom reorganization that do not produce changes in small angle scattering suggests that the observed small angle differences are not directly linked to the structural change reported at higher angles. Instead, we would suggest that the small angle changes arise from an oxidation state-dependent modulation of interparticle interactions that are not fully screened in these relatively concentrated cytochrome *c* solutions, even at high ionic strength. A variation in the interparticle interaction that slightly perturbs scattering in the small angle region, and would have a much smaller effect on high angle scattering data.

Temperature-Dependent Changes and Protein Dynamics in High Angle Scattering. Experimental results presented here, and previous computational studies (*31*), show that temperature-dependent changes in protein conformation and dynamics are manifest in high angle X-ray scattering data. Thermal factors and incoherent, liquidlike or rigid-body motions in proteins have been identified to significantly effect Bragg diffraction intensities and produce X-ray diffuse scattering in crystals (*36*, *45*−*47*). Numerical calculations of scattering patterns based upon atomic models show that thermal motions will also significantly affect high angle solution scattering. For example, the inclusion of crystallographic temperature factors in calculations of protein scattering patterns results in a modification of scattering amplitudes in a *q*-dependent manner, with negligible effects calculated in the small angle region ($q < 0.3$ Å^{-1}), but with increasing impact at high angles (*31*). The primary effect of atomic Debye−Waller factors on macromolecular scattering is calculated to be an increase in the drop-off of scattered intensity at high angles, lowering the level of high angle scattering compared to the small angle, $I(0)$ amplitude (*31*). This effect is opposite to the experimentally observed temperature induced high angle changes that we measured for cytochrome *c*.

Experimentally, temperature-dependent changes are observed in high angle scattering for cytochrome *c*, even in the temperature region between 1 and 25 °C far from denaturation. Increases in temperature were found to weaken the high angle undulatory scattering patterns, and to raise the high angle diffuse scattering levels compared to the $I(0)$ scattering amplitude. A similar trend was seen the temperature-dependent scattering for lysozyme (*49*), and for surfactant mobility-dependent changes in micelle scattering (*44*). The temperature-induced weakening of the high angle undulatory features combined with an increase in the level of the high angle diffuse scattering cannot be duplicated in calculations of scattering patterns by increasing individual atomic temperature factors alone. Instead, in the case of micelle scattering, we found that the effect of surfactant mobility on high angle scattering required inclusion of a Debye term for the atomic group defined by the surfactant molecule (*44*). This approximation makes physical sense since the surfactant molecule can be considered to be incoherently positioned with respect to a constant micelle structure (*50*). This approximation is analogous to the analysis of crystallographic data in terms of terms of a static, time-averaged structure that produces Bragg diffraction, with liquidlike or incoherent rigid-body motions that create diffuse scattering (*36*, *45*, *46*−*48*). We anticipate that methods of this type will also be needed to account for high angle scattering for proteins in solution. A more detailed examination of methods to account for protein dynamics in high angle scattering will be examined in an separate report. Main points to be made here that high angle difference scattering patterns are found to be sensitive to changes in protein conformation states, as indicated by oxidation state- and temperature-dependent changes in cytochrome *c* scattering, and that these difference scattering patterns can be quantitatively compared to detailed structural models. These results suggest that difference high angle scattering can be used to follow reaction-linked changes in protein structure and dynamics. This technique offers promise for providing a new, widely applicable technique for exploring conformational states linked to physiological protein function.

ACKNOWLEDGMENT

The authors are indebted to P. Thiyagarajan for his help and suggestions in preliminary experiments, and to Hiro Tsuruta for his help and input in collecting data at SSRL, and to the APS-BESSRC staff, especially Jennifer Linton, Mark Beno, Guy Jennings, and Mark Engbretson.

REFERENCES

1. Zhou, H.-X., Wlodek, S. T., and McCammon, J. A. (1998) *Proc. Natl. Acad. Sci. U.S.A. 95*, 9280−9283.
2. Frauenfelder, H., McMahon, B. H., Austin, R. H., Chu, K., and Groves, J. T. (2001) *Proc. Natl. Acad. Sci. U.S.A. 98*, 2370−2374.
3. Harrenga, A., Reincke, B., Ruterjans, H., Ludwid, B., and Michel, H. (2000) *J. Mol. Biol. 295*, 667−678.
4. Wagner, G., Hyberts, S. G., and Havel, T. F. (1992) *Annu. Rev. Biophys. Biomol. Struct. 21*, 167−198.
5. Billeter, M. (1992) *Quart. Rev. Biophys. 25*, 325−377.
6. Churg, A. K., Weiss, R. M., Warshel, A., and Takano, T. (1983) *J. Phys. Chem. 87*, 1683−1694.
7. Muegge, I., Qi, P. X., Wand, A. J., Chu, Z. T., and Warshel, A. (1997) *J. Phys. Chem. 101*, 825−836.
8. Trewhella, J., Carson, V. A. P., Curtis, E. H., and Heidorn, D. B. (1988) *Biochemistry 27*, 1121−1125.
9. Zhao, D., Hutton, H. M., Gooley, P. R., MacKenzie, N. E., and Cusanovich, M. A. (2000) *Protein Sci. 9*, 1828−1837.
10. Telford, J. R., Wittung-Stafshede, P., Gray, H. B., and Winkler, J. R. (1998) *Acc. Chem. Res. 31*, 755−763.
11. Berghuis, A. M., and Brayer, G. D. (1992) *J. Mol. Biol. 223*, 959−976.
12. Salemme, F. R., Freer, S. T., Xuong, N. H., Alden, R. A., and Kraut, J. (1973) *J. Biol. Chem. 248*, 3910.
13. Matsuura, Y., Takano, T., and Dickerson, R. E. (1982) *J. Mol. Biol. 156*, 389.

14. Qi, P. X., Beckman, R. A., and Wand, A. J. (1996) *Biochemistry 35*, 12275−12286.
15. Banci, L., Bertini, I., Gray, H. B., Reddig, T., Rosato, A., and Turano, P. (1997) *Biochemistry 36*, 9867−9877.
16. Banci, L., Bertini, I., Huber, J. G., Spyroulias, G. A., and Turano, P. (1999) *J. Biol. Inorg. Chem. 4*, 21−31.
17. Svergun, D. I., Burkhardt, N., Pedersen, J. S., Koch, M. H. J., Volkov, V. V., Kozin, M. B., Meerwink, W., Stuhrmann, H. B., Diedrich, G., and Nierhaus, K. H. (1997) *J. Mol. Biol. 271*, 602−618.
18. Svergun, D. I., Volkov, V. V., Kozin, M. B., Stuhrmann, H. B., Barberato, C., and Koch, M. H. J. (1997) *J. Appl. Crystallogr. 30*, 798−802.
19. Grossmann, J. G., and Hasnain, S. S. (1997) *J. Appl. Crystallogr. 30*, 770−775.
20. Chacon, P., Moran, F., Diaz, J. F., Pantos, E., and Andreu, J. M. (1998) *Biophys. J. 74*, 2760−2775.
21. Svergun, D. I. (1999) *Biophys. J. 76*, 2879−2886.
22. Walther, D., Cohen, F. E., and Doniach, S. (2000) *J. Appl. Crystallogr. 33*, 350−363.
23. Svergun, D. I., Malfois, M., Koch, M. H. J., Wigneshweraraj, S. R., and Buck, M. (2000) *J. Biol. Chem. 275*, 4210−4212.
24. Svergun, D. I., Volkov, V. V., Kozin, M. B., and Stuhrmann, H. B. (1996) *Acta Crystallogr. A52*, 419−426.
25. Chacon, P., Diaz, J. F., Moran, F., and Andreu, J. M. (2000) *J. Mol. Biol. 299*, 1289−1302.
26. Svergun, D. I., Petoukhov, M. V., and Koch, M. H. J. (2001) *Biophys. J. 80*, 2946−2953.
27. Seifert, S., Winans, R. E., Tiede, D. M., and Thiyagarajan, P. (2000) *J. Appl. Crystallogr. 33*, 782−784.
28. Fedorov, B. A., Krober, R., Damaschun, G., and Ruckpaul, K. (1976) *FEBS Lett. 65*, 92−95.
29. Fedorov, B. A., and Denesyuk, A. I. (1978) *J. Appl. Crystallogr. 11*, 473−477.
30. Svergun, D., Barberato, C., and Koch, M. H. J. (1995) *J. Appl. Crystallogr. 28*, 768−773.
31. Zhang, R., Seifert, S., Thiyagarajan, P., and Tiede, D. M. (2000) *J. Appl. Crystallogr. 33*, 565−568.
32. Zhang, R., Thiyagarajan, P., and Tiede, D. M. (1999) in *Materials Research Using Cold Neutrons at Pulsed Neutron Sources Conference* (Thiyagarajan, P., Trouw, F. R., Marzec, B., and Loong, C.-K., Eds.) pp 214−219, World Scientific Publishing Co., Inc., New Jersey.
33. Cotton, J. P. (1991) in *Neutron, X-ray and Light Scattering* (Lindner, P., and Zemb, T., Eds.) pp 3−18, Elsevier Science Publishers B.V., Amsterdam.
34. Ducruix, A., Guilloteau, J. P., Ries-Kautt, M., and Tardieu, A. (1996) *J. Cryst. Growth 168*, 28−39.
35. Tiede, D. M., and Thiyagarajan, P. (1996) in *Biophysical Techniques in Photosynthesis* (Amesz, J., and Hoff, A. J., Eds.) pp 375−390, Kluwer Academic Publishers, Dordrecht.
36. Warren, B. E. (1990) *X-ray Diffraction*, Dover Publications, Inc., New York.
37. Fraser, R. D. B., MacRae, T. P., and Suzuki, E. (1978) *J. Appl. Crystallogr. 11*, 693−694.
38. Berman, H. M., Westbrook, J., Feng, Z., Gilliland, G., Bhat, T. N., Weissig, H., Shindyalov, I. N., and Bourne, P. E. (2000) *Nucleic Acids Res. 28*, 235−242.
39. Louie, G. V., and Brayer, G. D. (1990) *J. Mol. Biol. 214*, 527−555.
40. Bushnell, G. W., Louie, G. V., and Brayer, G. D. (1990) *J. Mol. Biol. 214*, 585−595.
41. Chen, S. H., and Bendedouch, D. (1986) *Methods Enzymol.*, 13079−13116.
42. Feng, Y., Roder, H., and Englander, S. W. (1990) *Biochemistry 29*, 3494−3504.
43. Guinier, A., and Fournet, G. (1955) *Small Angle Scattering*, Wiley, New York.
44. Zhang, R., Marone, P. A., Thiyagarajan, P., and Tiede, D. M. (1999) *Langmuir 22*, 7510−7519.
45. Caspar, D., Clarage, J., Salunke, D., and Clarage, M. (1988) *Nature 332*, 659−662.
46. Benoit, J., and Doucet, J. (1995) *Quart. Rev. Biophys. 28*, 131−169.
47. Hery, S., Genest, D., and Smith, J. C. (1998) *J. Mol. Biol. 279*, 303−319.
48. Wall, M. E., Ealick, S. E., and Gruner, S. M. (1997) *Proc. Natl. Acad. Sci. U.S.A. 94*, 6180−6184.
49. Arai, S., and Hirai, M. (1999) *Biophys. J. 76*, 2192−2197.
50. Palmer, B. J., Liu, J., and Virden, J. (1999) *Langmuir 15*, 7426−7431.
51. Diamond, R. (1974) *J. Mol. Biol. 82*, 371−391.
52. Evans, S. V., and Brayer, G. D. (1990) *J. Mol. Biol. 213*, 885−897.

BI015931H